Article

Optoelectronic Properties of Ultrathin Indium Tin Oxide Films: A First-Principle Study

Xiaoyan Liu, Lei Wang * and Yi Tong *

College of Electronic and Optical Engineering & College of Microelectronics, Nanjing University of Posts and Telecommunications, Nanjing 210023, China; xiaoyanliu@njupt.edu.cn
* Correspondence: LeiWang1980@njupt.edu.cn (L.W.); tongyi@njupt.edu.cn (Y.T.)

Abstract: First-principle density functional theory simulations have been performed to predict the electronic structures and optoelectronic properties of ultrathin indium tin oxide (ITO) films, having different thicknesses and temperatures. Our results and analysis led us to predict that the physical properties of ultrathin films of ITO have a direct relation with film thickness rather than temperature. Moreover, we found that a thin film of ITO (1 nm thickness) has a larger absorption coefficient, lower reflectivity, and higher transmittance in the visible light region compared with that of 2 and 3 nm thick ITO films. We suggest that this might be due to the stronger surface strain effect in 1 nm thick ITO film. On the other hand, all three thin films produce similar optical spectra. Finally, excellent agreement was found between the calculated electrical resistivities of the ultrathin film of ITO and that of its experimental data. It is concluded that the electrical resistivities reduce along with the increase in film thickness of ITO because of the short strain length and limited bandgap distributions.

Keywords: ITO; optoelectronic; first-principle calculation

1. Introduction

Recently, transparent conducting oxide (TCO) films have been employed in widespread commercial applications due to their high electrical conductivity and high optical transparency in the visible range [1]. Indium tin oxide (ITO) is a typical TCO which has a wide bandgap of ~3.8 eV and high transparency (> 80%) in the visible range [2]. These superior physical characteristics are responsible for its wide range of applications in some mainstream optoelectronic devices such as touch screens, flat panel displays, solar cells, and defrosters [3–6]. Moreover, ITO films have also been used in the emerging phase-change photonic devices, where they protect the phase-change layer from oxidation and sustain sufficient thermal energy for the required phase transformation [7–9]. So, it is necessary to accurately predict and optimize the optoelectronic properties of ITO films that can dramatically affect the computation and storage performances of these novel photonic devices.

Density functional theory (DFT) simulations can effectively determine the structural, optical, and electronic properties of ITO materials [10–12]. However, there is little agreement between theory and experimental measurements. For instance, the simulated uniform inward relaxation value of Sn atoms in ITO (in the first coordination shell) is 0.10 Å [13], which is much lower than that of the experimentally measured averaged relaxation value of 0.18 Å [14]. Besides the structural disparities between the simulations and experiments, the calculated electronic structure of ITO has different positioning of energy levels compared with that of experimental data [15]. So, that is why the simulated and observed optical spectra do not match each other [16,17]. It is reported that such discrepancies are due to the underestimation of the binding energy of localized In 4d levels within the standard DFT calculations [18], which are also reflected in the calculated electronic structure of the ITO media [16]. To closely mimic the practical environment and solve the above issue, one promising route to solve such problems is to include the on-site corrections within

the DFT+U framework [10,11,19]. With the help of DFT+U simulations, we can accurately calculate the average inward relaxation value (0.16 Å) of Sn around its atoms, which has a nice correlation with that of the experimental value of 0.18 Å [10]. Moreover, the electronic structure of ITO can be accurately calculated using the DFT+U scenario, thereby leading to good agreement between the calculated optical transmission and its experimental observations [19].

Although significantly advanced levels of theoretical frameworks (DFT) of ITO have been reported for ITO, most of these reports largely focus on the bulk optoelectronic properties of ITO with a film thickness of >10 nm. In addition, the continuous downscaling of phase-change photonic devices necessitates an ultrathin ITO-coated layer with a thickness of <5 nm [20,21]. The optoelectronic properties of this type of thin film are rarely reported, both experimentally and theoretically. So, an ITO environment for the aforementioned DFT calculation is considered at the vacuum level, which is obviously deviating from the practical setup that usually suffers from large joule heating [22]. In order to address these issues and provide the characteristics of the realistic materials for future device optimization, a sophisticated theoretical framework has been proposed. In this framework, ultrathin films of ITO were considered for DFT simulations and subsequently implemented to assess the structure as well as electronic and optical properties of this material at different thicknesses (i.e., 1, 2, and 3 nm) under temperatures varying from 100 to 600 K that covers a wide range of possible reported values [7,8,21].

2. Materials and Methods

DFT calculations were performed for ITO films of different thicknesses, which were subsequently utilized to find the optimized ITO structures at various temperatures. The Vienna ab initio Simulation Package (VASP) [23,24] was employed for the DFT simulations. The optical properties were calculated with the DFT+U approach, with a value of U = 7 eV [25,26]. The ITO structure was constructed based on the In_2O_3 cell from the Material Project Database, where two In atoms are substituted by Sn atoms. To maintain the electroneutrality of the ITO structure, an extra O atom was incorporated into the system. We utilized the mp-22598 In_2O_3 from Materials Project [27]. The space group was IA, and the chemical composition of the cell was $In_{32}O_{48}$. In our calculation, we chose a (001) surface and the surface was terminated with In atoms. The vacuum layer was set to be larger than 10 Å. The cut-off energy of 400 eV and Perdew–Burke–Ernzerhof (PBE) functional with the generalized gradient approximation (GGA) were adopted to describe the electronic properties of the ITO films [28,29]. The projector augmented wave (PAW) was employed to describe core–electron interactions [30,31]. The force threshold and energy threshold were set to 0.05 eV/Å and 10^{-4} eV, respectively. The lattice parameters for the proposed structure were optimized with a $1 \times 1 \times 1$ k-point due to the relatively large ITO structures, following the Monkhorst–Pack scheme [32]. The above configurations led to an optimized lattice constant of 10.3 Å, which well matched the experimental value of 10.08 Å [14]. As all the optimized lattice parameters were comparable to 1 nm, the optimized ITO cells were deployed to build $1 \times 1 \times 1$, $1 \times 1 \times 2$, and $1 \times 1 \times 3$ supercells, corresponding to 1, 2, and 3 nm ITO structures (see Figure 1), respectively. Ab initio molecular dynamic (AIMD) simulations were used to obtain structures at different temperatures and to equilibrate the considered systems. The aforementioned settings in DFT calculations were also applied to AIMD calculations in the ab initio part, and here we used a Nosé–Hoover thermostat for the MD calculations. The time step was set to 1.25 fs. Initially, the proposed ITO structures (i.e., 1, 2, and 3 nm thicknesses) underwent relaxation at 800 K for 5000 fs, which is adequately long to attain the fully converged structures and equilibrate at high temperatures. Later on, the obtained structures were subsequently annealed with a reasonable velocity of 0.4 K/fs to 100, 200, 300, 400, 500, and 600 K, respectively. It is necessary to mention that the calculated ITO thickness is restricted to be 3 nm due to the limitation of the theoretical method. In DFT calculations, the computational time increases exponentially with the increase of atom numbers in a system, resulting in the upper limit of 3 nm in our work.
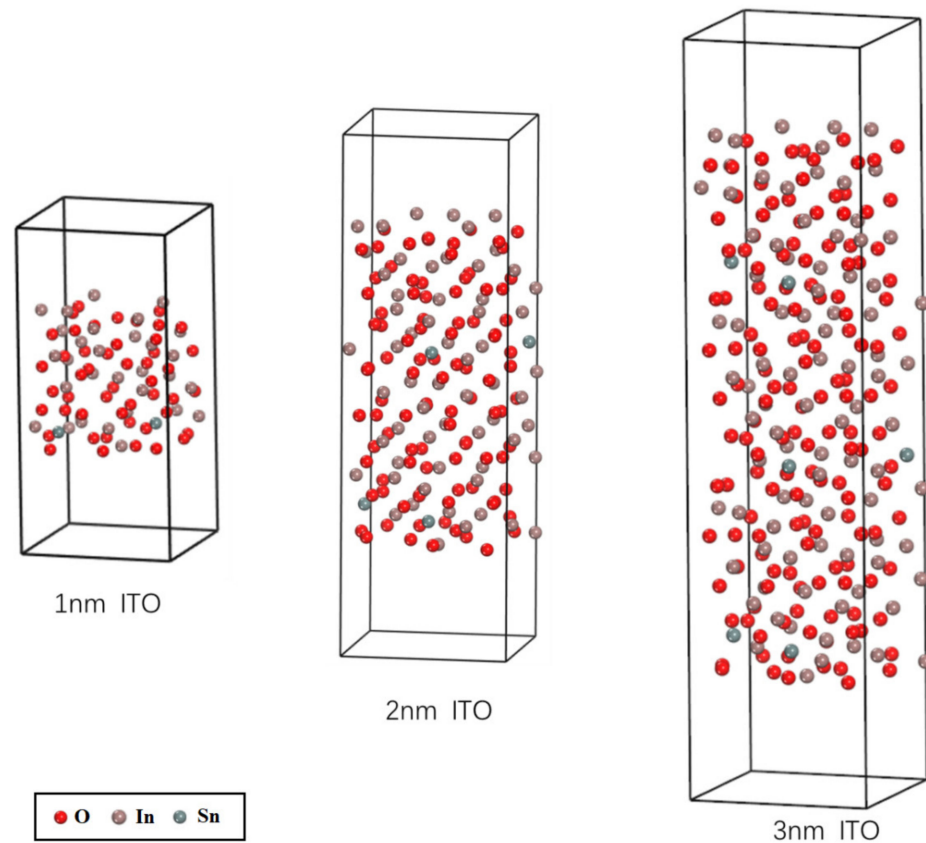
Figure 1. Simulated structures of indium tin oxide (ITO) with different thicknesses. The atomic structures are extracted from the molecular dynamics calculations at a random step.

The optimized structures were further used to calculate the electric resistivities of the ITO films at different thicknesses and temperatures according to the openMX package [33–36]. The modeling parameters in the openMX package were set to be similar or even more accurate when compared with those adopted in VASP. Although, the GGA-PBE functional was still adopted by openMx, the cut-off energy was increased to 150 Ry (2040 eV), which was due to the required higher cut-off energy for orbital mixing. In this case, the energy threshold was set to be 10^{-7} Hartree (2.7×10^{-6} eV) [37].

3. Results and Discussions

3.1. Electronic Structure Properties of Ultrathin Films of ITO

The electronic structures of ultrathin films of ITO were first studied to reveal the microscopic view at the atomistic level. The total density of states near the Fermi level (-5 to 5 eV) is illustrated in Figure 2, where we can see the strongest peak at -2 eV. In addition, the valence band Density of States (DOS) (-4 to 0 eV) of all these peaks is much higher than that of the conduction band DOS (0–4 eV). Comparative analysis of these figures led us to predict that the region near the Fermi level is mostly occupied, which is responsible for strong bonding properties. Moreover, these peaks exist under various temperatures and thicknesses, which results in the good stability of the proposed structures. Furthermore, the 1 nm thick ITO structure has a smaller DOS in the conduction band region (0–5 eV), which is due to the partial hybridization of the antibonding orbitals. On the other hand, less pronounced peaks are found in the same region for the 2 and 3 nm thick ITO structures. This discrepancy implies that the electrons in 1 nm ITO are more likely to be located in the region of -5 to 5 eV, while those of 2 and 3 nm thick ITO structures exist in the range of -5 to 0 eV. It was found that the total density of states (TDOS) of 1 nm ITO at various temperatures have different shapes, showing a temperature-sensitive electronic structure. This effect of temperature is not obvious in the case of 2 and 3 nm thick ITO, where the

varying temperature changed the peak intensity rather than the peak position. The reason behind this is the smaller number of atoms in 1 nm thick ITO compared with that of the 2 and 3 nm cases. It is evident that the structures with more atoms can effectively offset the error between different structural fluctuations caused by temperature variations.
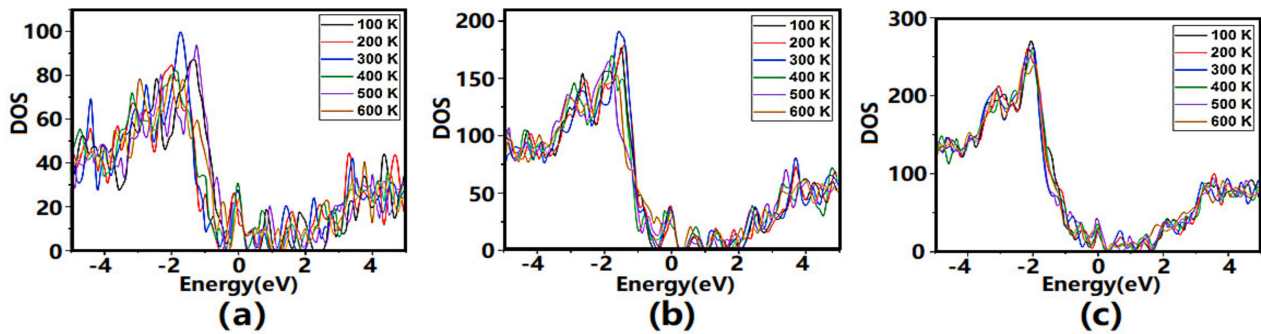

Figure 2. Total density of states (TDOS) of 1 nm (**a**), 2 nm (**b**), and 3 nm (**c**) ITO models near the Fermi level (−5 to 5 eV) at temperatures ranging from 100 to 600 K.

The projected density of states (PDOS) of these three ITO films was also calculated, as illustrated in Figure 3. In the case of 1 nm ITO, the shape of the In PDOS is wide and smooth at −5 to −1 eV, and the main contribution is from its 4d bonding orbitals. Moreover, we also found a broad and weak band in the energy range of −18 to −16 eV, which is attributed to the bonding orbitals of In 5s and 5p orbitals, responsible for their wide energy span. The PDOS of O is also strong in the valance band region (~ −1.8 eV), which shows the formation of strong metal–oxygen bonds. Most of the PDOS of Sn atoms have a peak at −5 to −4 eV, which is much deeper than the main peak of In. This result may suggest that the doping of Sn into the In_2O_3 structure is favorable and produces a stable species. The electron densities (obtained from the PDOS) of 1 nm ITO at different temperatures are around the Fermi level, which results in a very small bandgap for 1 nm ITO. In the case of 2 and 3 nm ITO structures, similar band positions of Sn, In, and O elements are observed. The only difference in the PDOS plots of these structures is interpreted in the form of the density variation, which is in the region of 0–5 eV (Figure 3). The 1 nm ITO has a low density in this region, while a small increase was found for the 2 and 3 nm ITO cases. This is responsible for the increased intensity of antibonding orbitals in the conduction band region. In the energy regions of −5 to −4 eV, the PDOS of Sn are relatively higher than those in the range of −2 to 0 eV. There are two possible reasons to explain such an effect. On the one hand, there are only two Sn atoms in the system, and their PDOS may be "submerged" into the PDOS of pristine In_2O_3. Hence, the shape of Sn PDOS may be different from that of In or O. On the other hand, although the peaks in −5 to −4 eV are higher, there are still peaks in the range of −2 to 0 eV, meaning that Sn atoms interact with the surrounding environment and the electron density overlaps with those atoms. The band structures of the proposed ITO films were also calculated, which are given in Figure 4. The results of TDOS and band structure are similar; so, here, only one certain band at 100 K is discussed. The simulated bandgap of 1 nm ITO is ~0.8 eV above the Fermi level, which results in its semiconducting nature. The band structure of the 2 nm ITO at 100 K is similar to that of the 1 nm ITO but with a large number of bands. This large number of bands may be due to a large number of atoms inside the 2 nm layer. These atoms would have a stronger interatomic effect, forming new and complex bands within the overall energy range, especially near the Fermi level. So, these extra band occupations near the Fermi level diminish the bandgap and yield a negligible gap of 0.1 eV. Similarly, the 3 nm ITO has more atoms; so, a severe situation is observed, where a large number of atoms contribute to the overall band distribution and result in a much narrower bandgap, as shown in Figure 4. Comparative analysis of the data of Figure 2; Figure 4 leads us to conclude that ultrathin films of ITO exhibit narrow bandgaps that eventually disappear with film thickness. The

complex band formation near the Fermi levels of 2 and 3 nm ITO structures can enhance the electron transfer property. Thus, it was found that the thicker ITO layer has a lower resistivity and higher electrical conductivity.
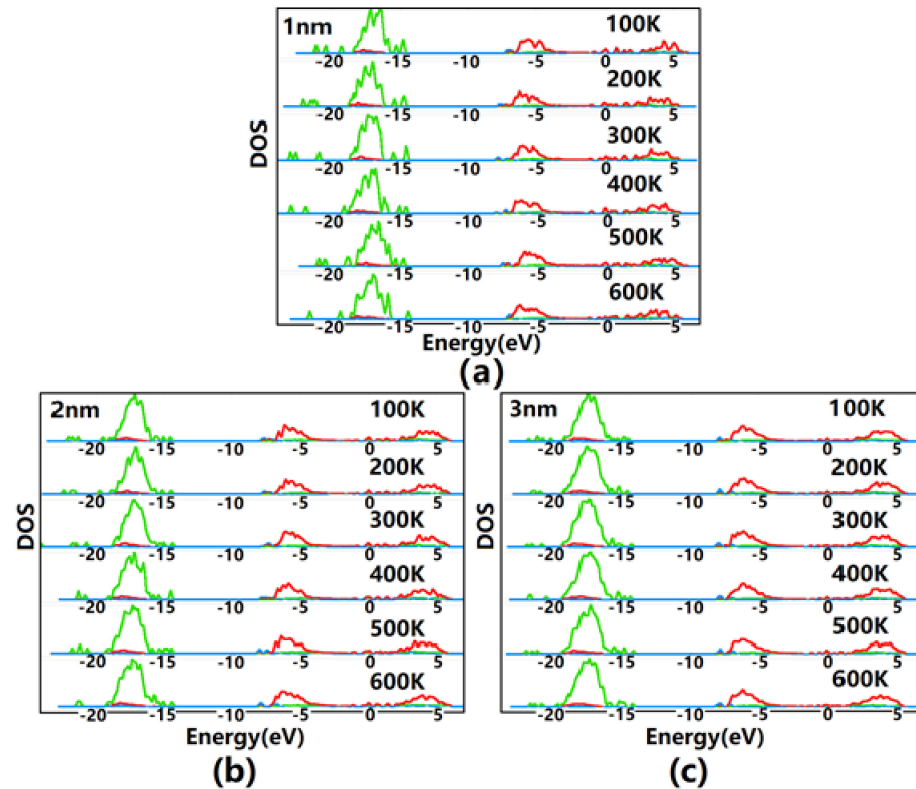

Figure 3. Projected density of states (PDOS) of the ITO films with thicknesses of 1 nm (**a**), 2 nm (**b**), and 3 nm (**c**) at temperatures varying from 100 to 600 K over Sn, O, and In atoms. PDOS over In, O, and Sn atoms are denoted by red, green, and blue colors.
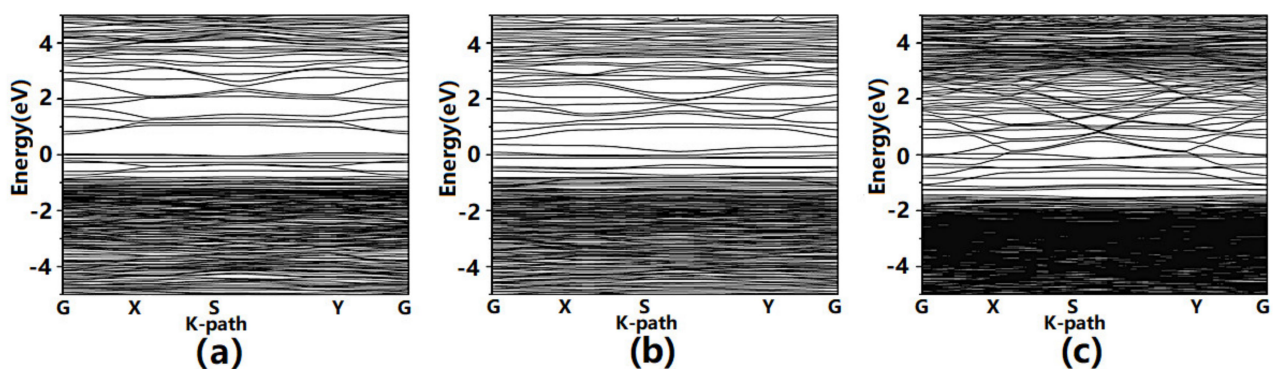

Figure 4. Band structures of 1 nm (**a**), 2 nm (**b**), and 3 nm (**c**) ITO near the Fermi level (−5 to 5 eV) at 100 K.

The developed DFT model was further utilized to calculate the surface energy of the ultrathin ITO films, and the results are shown in Figure 5. To study the surface strain effect, we calculated the surface energy γ (unit in eV/Å^2) by the formula given below:

$$\gamma = \frac{E_{slab} - N \cdot E_{bulk}}{2A} \tag{1}$$

where E_{slab} represents the total energy of a slab structure of ITO (e.g., 1, 2, and 3 nm ITO structures), N indicates the ratio of atom numbers between the slab ITO structure and the

bulk ITO structure, and E_{bulk} represents the total energy of the bulk ITO structure. A shows the surface area of the proposed slab structure, and the coefficient 2 is considered as the slab of the ITO structure with top and bottom exposed surfaces. From Figure 5, we can see that the surface energy increases along with the increase in thickness of ITO at different temperatures. This statement is contradictory to common sense, namely, that thicker films have lower surface energies than those of thinner ones [38]. The reason behind this may be the involvement of just two Sn atoms as dopants in 1 nm ITO, which are less susceptible to the system energy. However, more Sn atoms are incorporated in the thicker ITO films, which produce large displacement during the molecular dynamics calculation, which may affect the optimization (DFT) process as well. The ITO system with fewer Sn atoms is more stable. So, this may imply that the ultrathin ITO system is more stable than the thicker structures, incapable of providing sufficient vacancies or electron holes to conduct the electron transfer. In addition, the surface energy gradually increases along with the increase in temperature. This may be readily attributed to the more drastic perturbation of the system caused by higher temperatures.
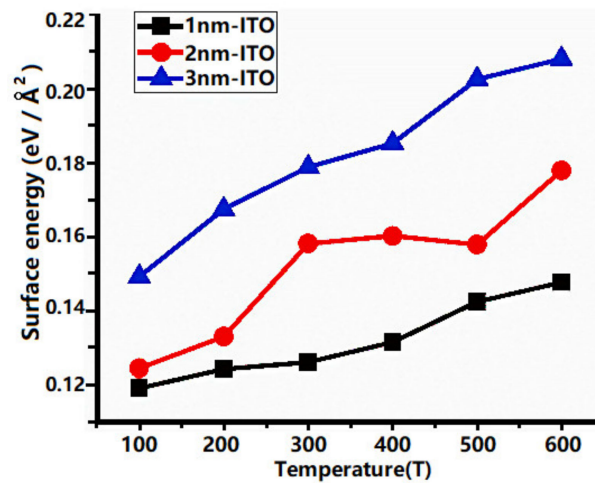

Figure 5. Surface energy of 1, 2, and 3 nm ITO models at temperatures ranging from 100 to 600 K.

3.2. Optical Properties of Ultrathin Films of ITO

We have also simulated the optical properties of the ultrathin films of ITO using the developed DFT method. To obtain the optical properties (e.g., refractive index) of the ITO film, we first calculated the imaginary parts (ε_1) and real parts (ε_2) of the dielectric constant via

$$\varepsilon_1(\omega) = 1 + \frac{2e}{\varepsilon_0 m^2} \cdot \sum_{V.C} \int \frac{2dK}{(2\pi)^2} \frac{|a \cdot M_{V.C}(K)|^2}{\frac{[E_C(K) - E_V(K)]}{\hbar}} \cdot \frac{1}{\frac{[E_C(K) - E_V(K)]^2}{\hbar^2} - \omega^2}, \tag{2}$$

$$\varepsilon_2(\omega) = \frac{\pi}{\varepsilon_0}\left(\frac{e}{m\omega}\right)^2 \cdot \sum_{V.C} \int_{BZ} \frac{2dK}{(2\pi)^2} |a \cdot M_{V.C}|^2 \delta[E_C(K) - E_V(K) - \hbar\omega], \tag{3}$$

where ε_0 is the dielectric constant in vacuum, ω is the angular frequency, C is the conduction band, V is the valence band, BZ is the first Brillouin zone, K is the electron wave vector, a is the unit direction of the vector potential A, $M_{V.C}$ is the transition matrix element, and the vectors $E_C(K)$ and $E_V(K)$ are the intrinsic energy levels on the conduction band and the valence band, respectively. The total dielectric constant has the equality $\varepsilon = \varepsilon_1 + i\varepsilon_2$. The values of ε_1 and ε_2 can be obtained through DFT calculations, and thus the total dielectric constant is subsequently attained. All the optical properties in this work were therefore calculated based on these two values.

The absorption coefficients of the proposed structures are shown in Figure 6. Comparative analysis of the data of Figure 6 led us to predict that 1 nm ITO has lower adsorption

coefficients than those of the 2 and 3 nm systems. Since the adsorption coefficient describes the extent of light intensity decay through the film, the lower absorption coefficients found on the 1 nm ITO structure simply suggest its low quantum efficiency. However, we found that 1 nm ITO thin film has some peaks in the visible region (1.63–3.11 eV) (bottom panel of Figure 6), which indicates its excellent visible light absorption capability. On the other hand, no such peaks are found for 2 and 3 nm ITO structures. In addition, the effect of temperature is minor on the absorption coefficients of all three systems. Considering that the calculated temperature range (100–600 K) is relatively low, the atoms of ITO inside the thin film may probably undergo weak thermal vibration, resulting in a similar thermal motion mode for different temperatures. This consequently leads to the comparable long-range structure order, which is analogous to the optical properties at different temperatures for a given thickness.
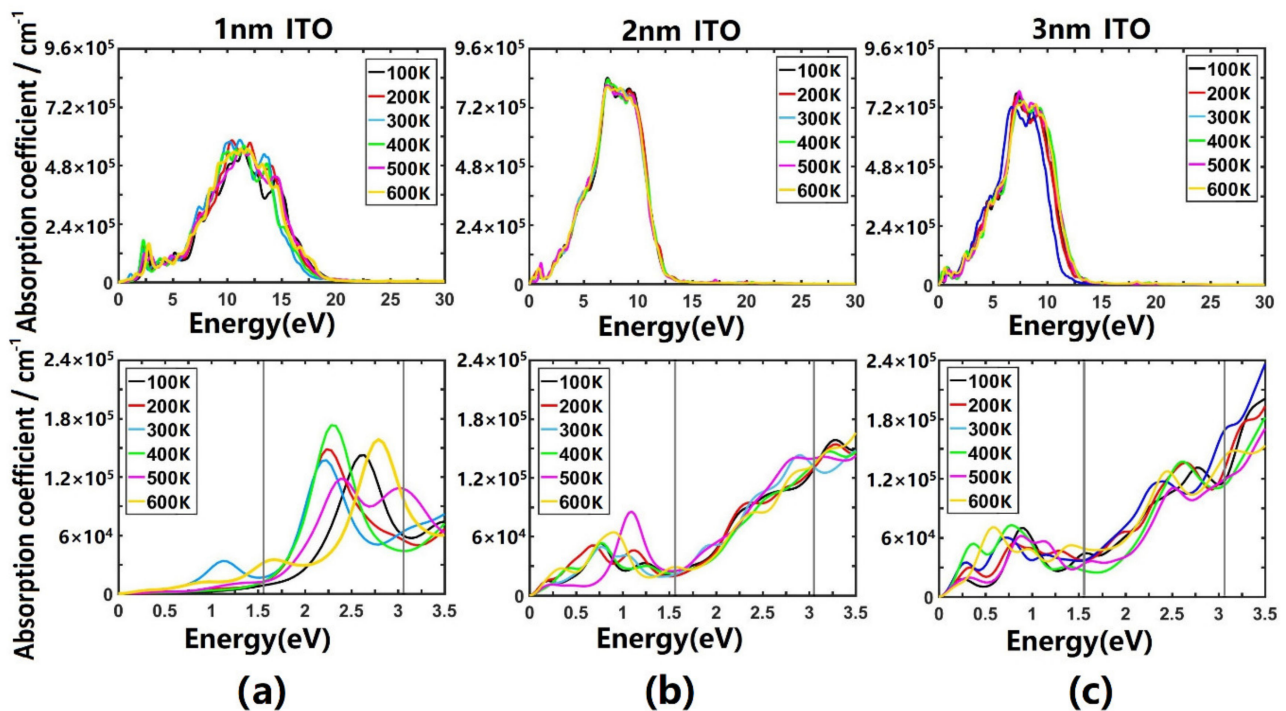

Figure 6. Absorption coefficient (in cm^{-1}) spectra of 1 (**a**), 2 (**b**), and 3 (**c**) nm ITO models at temperatures ranging from 100 to 600 K. Upper panel shows the spectra in the energy range between 0 and 30 eV. The lower panel highlights the region near the visible light zone bounded by two gray dashes (energy varies from 1.63 to 3.11 eV).

The reflectivity and complex refractive index of the considered models at different thicknesses and temperatures were subsequently calculated and are illustrated in Figure 7. Similar to the results of absorption coefficients, 1 nm ITO has a lower reflectivity than that of 2 and 3 nm configurations (see Figure 7a). This statement further confirms the better absorption property of 1 nm ITO. Such reflectivity variations at different thicknesses are due to the surface strain effects, which compress the ITO structure and thus increase the chance of photon collision with the film. The complex reflective index ($n(\omega)$) (Figure 7b) strongly relates the real and imaginary parts of the complex dielectric constant, which is defined elsewhere [39]:

$$n(\omega) = \frac{1}{\sqrt{2}}[(\varepsilon_1^2 + \varepsilon_2^2)^{1/2} + \varepsilon_1]^{1/2} \tag{4}$$

where ω is the frequency, and ε_1 and ε_2 are the real and imaginary parts of the calculated complex dielectric constants of the ITO film at different conditions, respectively. It is clear that the values of the complex refractive index vary between 0.5 and 2.5 for all three structures of different thicknesses while being less sensitive to temperature. The 1 nm ITO

structure exhibits a sharp peak in the energy range of ~1.3 eV, which is absent in the 2 and 3 nm structures. Moreover, a broad peak was found to be located at ~4.2, ~2.7, and ~2.1 eV for 1, 2, and 3 nm ITO structures, respectively, while their respective refractive index was calculated to be ~1.6, ~1.8, and ~1.9, respectively. Considering that these peaks mainly lie in the visible region of light, it is very likely that the 1 nm ITO film will generate a relatively smaller refractive index than that of the other two systems. The temperature-independent refractive index and absorption spectra can be also interpreted by the Kubo formula, which is usually adopted to calculate the optical conductivity [40]:

$$\chi_1^{ab}(-\omega, \omega) = \frac{e^2}{\hbar} \int \frac{dk}{8\pi^3} \sum_{n,m} \frac{f_{nm} r_{nm}^a r_{mn}^b}{(\omega_{mn} - \omega - i\eta)} \tag{5}$$

where the summation is over band indices n and m, r_{nm} is the Berry connection, and f_{nm} is the difference in Fermi–Dirac distribution between bands n and m. The major terms that change with temperature are the distribution function, f_{nm}, and the small broadening factor $i\eta$, but these two parameters are changing on the scale of thermal energy $k_B T$, which is approximately 25.7 meV at room temperature. It is obvious that the temperature dependence trend becomes less apparent when the photon energy ω is much larger than $k_B T$ (i.e., in the visible range).
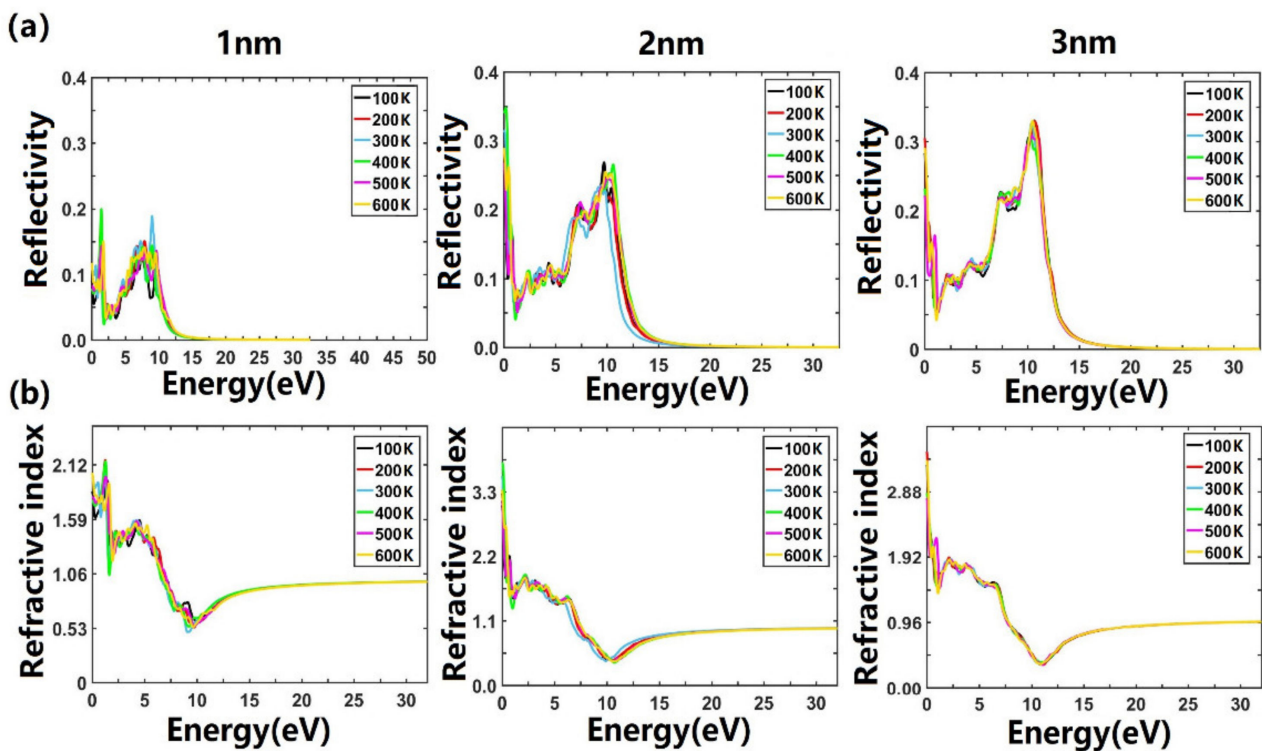

Figure 7. (**a**) Reflectivity spectra and (**b**) refractive index of 1, 2, and 3 nm ITO models at temperatures ranging from 100 to 600 K.

The calculated energy loss spectrum at various thicknesses of ITO and temperatures is shown in Figure 8a, where sharp peaks are present in the energy range of 10–16 eV. Such a peak for the 1 nm ITO at 100 K is situated at 15.5 eV, whereas the peak position of this band shifts to a low energy state along with higher temperatures, simultaneously augmenting the energy loss value of the peak. Therefore, the photon traveling is much more difficult in the 1 nm ITO structure as the temperature increases, implying a good photon absorption capability at low temperatures. However, the aforementioned behaviors are absent in 2 and 3 nm ITO structures. The 2 nm ITO configuration generates similar energy loss values in the range of 3.3–3.5 at ~13 eV for different temperatures. The peak values of all three

structures were calculated to be ~2.4, ~3.5, and ~4.5, respectively. This suggests that the thicker ITO film has weakened photon absorption capability. Considering the extinction coefficient of all three structures (Figure 8b), a sharp peak exists in the energy range of 5–10 for all three structures. The peak values of these three thicknesses are theoretically estimated to be 0.8, 1.0, and 1.1, respectively. This clearly indicates that the thicker ITO films have higher extinction coefficients. Furthermore, a sharp peak at ~2 eV was found in the 1 nm structure, the extinction coefficient of which gradually increases at the energy range from 0 to 2 eV, while there is no such peak in 2 and 3 nm ITO. The resulting peak information led us to predict a large extinction coefficient in the visible region of light.
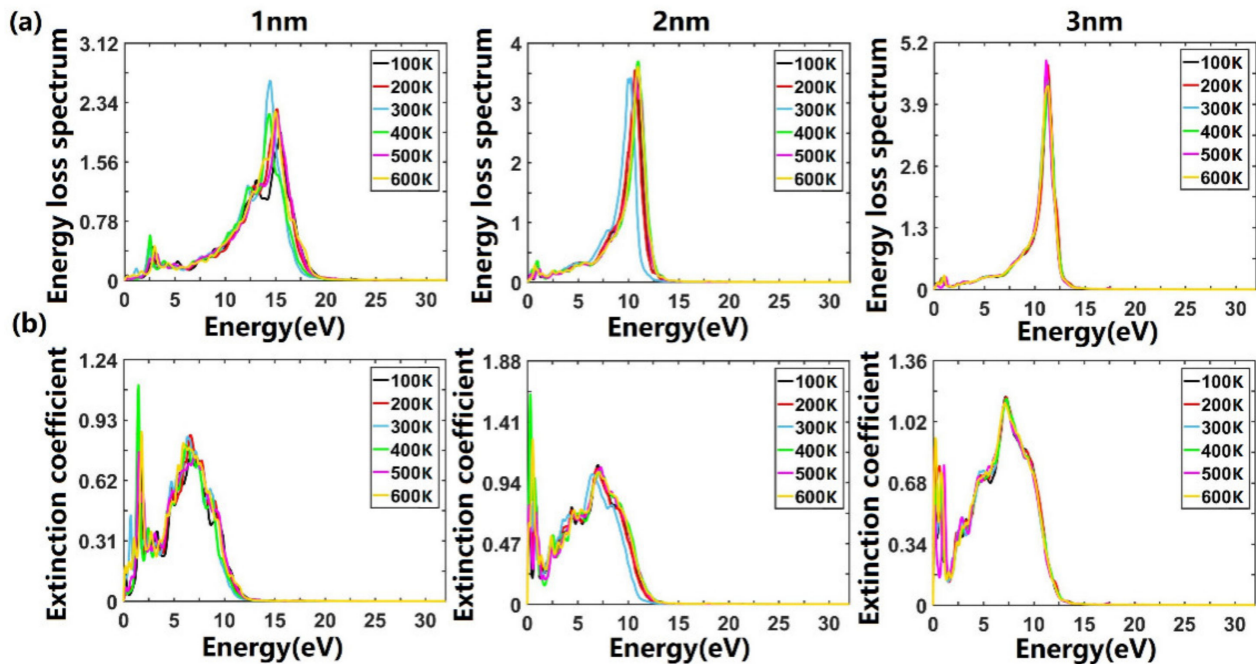

Figure 8. (**a**) Energy loss spectrum and (**b**) extinction coefficient of 1, 2, and 3 nm ITO models at temperatures such as from 100 to 600 K.

The photon transmittance of ITO film (*T*), which is schematically described in Figure 9, can be defined as follows [41]:

$$T = (1 - R)\exp^{-\alpha t}, \tag{6}$$

where *R*, α, and *t* denote reflectance, absorption coefficient, and film thickness, respectively. All of the investigated ITO structures give rise to high transmittance (>75%) in the visible light region (380–780 nm). This is also consistent with the experimental observations where the transmittance of ITO films is above 80% within the same wavelength range [41]. It was found that 1 nm ITO generally has higher transmittance than 2 and 3 nm ITO films in the visible light region. Owing to the thickness of ITO adopted here, the $e^{-\alpha t}$ term in this case is approximately equal to 1, and the calculated transmittance of the ITO film can be determined from its reflectivity using Equation (2). As a result, the smaller reflectivity of 1 nm ITO in the visible light region allows larger transmittance compared with that of thicker ones. Further, the transmittance of 1 nm ITO with a wavelength of >780 nm was found to be smaller than that of 2 and 3 nm ITO, which exhibit almost constant transmittance in the range from 200 to 1000 nm. These results and discussions led us to conclude that thicker ITO thin film has better light transmission in the near-infrared region.
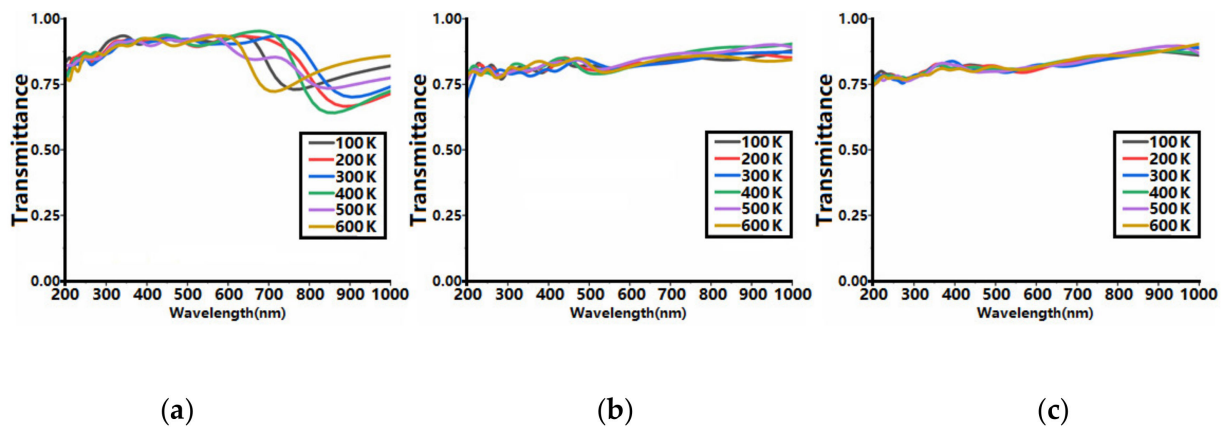
Figure 9. Transmittance spectra of 1 (**a**), 2 (**b**), and 3 nm (**c**) ITO models at temperatures ranging from 100 to 600 K.

3.3. Electrical Transport Properties of Ultrathin Films of ITO

The developed computational methods were employed for the first time to probe the electrical resistivity of ITO films at different thicknesses and temperatures, and the results are shown in Figure 10. The resistivity ρ can be evaluated through the formula ρ = RS/L, where R is the resistance, S is the area of the slab, and L is the length of the slab. The S and L values can be easily obtained from the structural information of the ITO model. Note that R is also determined by the Ohm's law (i.e., R = U/I), where U is the potential and *I* is the current. These two terms were calculated with the NEFG method implemented in OpenMX. To perform NEFG calculations, a finite bias voltage was first set to 0.5 V here, and the current was evaluated by

$$I_\sigma = \frac{e}{h} \int dE T_\sigma(E) \Delta f(E), \tag{7}$$

where T_σ is given by

$$T_\sigma(E) = \frac{1}{V_C} \int_{BZ} dk^3 T_\sigma^{(k)}(E), \tag{8}$$

where $T\sigma^{(K)}$ indicates the k-revolved transmission, which can be attained through the NEFG calculations.
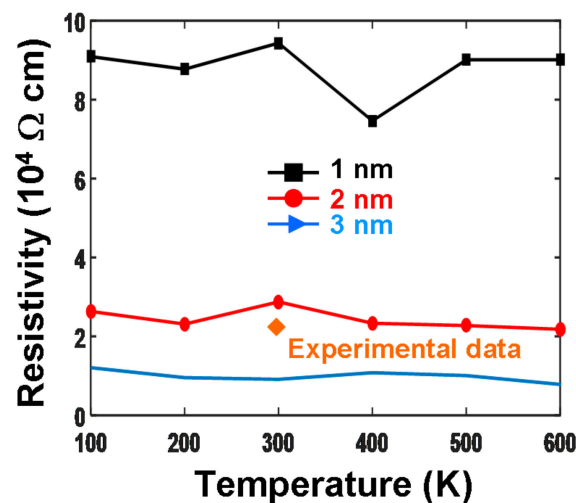

Figure 10. The plot of resistivity vs temperature ranging from 100 to 600 K of ITO structures at different thicknesses.

We found that the electrical resistivities of the ITO films at the proposed thicknesses are not liable to the temperature range of 100–600 K. Nevertheless, it is obvious that the thinner ITO (1 nm ITO) gives rise to larger resistivity when compared with the thicker ITO films (2 and 3 nm ITO). This result is also consistent with those of the reported ones [40]. The electrical resistivity of the 2 nm ITO layer was calculated to be ~3×10^4 (Ωcm), which shows good agreement with the experimental data of 2.11×10^4 (Ωcm) [42]. The main reason behind this discrepancy is the strain effect of ITO films. According to the simulations, the 1 nm ITO film is largely strained, with an average length of 0.96 Å at a temperature range of 100–600 K. On the other hand, 2 and 3 nm ITO films exhibit the average strain length of 0.99 and 1.01 Å, respectively. It can be therefore speculated that the thinner ITO film is highly strained, thus resulting in a shorter atomic bond length. Such shorter bonds may increase the free path of the electron transport, which consequently induces poor electrical conductivity. On the contrary, the strain impact on the thicker ITO films (similar to bulk ITO) is remarkably attenuated, consequently rendering the 2 and 3 nm ITO films less electrically resistive. In addition to the strain effect, the narrow bandgaps present the thicker inside of ITO films. These are likely to facilitate the carrier mobility and mitigate the electrical transport characteristic. The electrical conductivity can be defined as $\sigma = n_0 q \mu_n + p_0 q \mu_p$, where μ_n and μ_p correspond to the mobility of electron and hole, respectively, and n0 and p0 relate to the bandgap.

4. Conclusions

Density functional theory and nonequilibrium Green function methods have been employed to simulate the structural and optoelectronic properties of ultrathin films of ITO at different thicknesses (1–3 nm) and temperature (100–600 K). It was found that the calculated physical properties are immune to temperature and have a direct relation with the thickness of the film. The 1 nm thick ITO thin film has a larger absorption coefficient, low reflectivity, and higher transmittance in the visible light region compared with that of 2 and 3 nm ITO thin films. The reason behind this is the stronger surface strain effect in 1 nm thin film of ITO. However, all three systems have similar optical spectra. The calculated electrical resistivities of the ultrathin film of ITO are in good agreement with the experimental data. However, this correlation was found to be decreased along with the increase in film thickness, which is due to the short strain length and limited bandgap distributions.

Author Contributions: Conceptualization, L.W. and Y.T.; methodology, X.L.; software, X.L.; formal analysis, X.L., L.W., and Y.T.; writing—original draft preparation, X.L., L.W., and Y.T.; writing—review and editing, L.W. and Y.T.; supervision, L.W. and Y.T. All authors have read and agreed to the published version of the manuscript.

Data Availability Statement: The data presented in this study are available on request from the corresponding author.

Conflicts of Interest: The authors declare no conflict of interest.

References

1. Gokceli, G.; Karatepe, N. Improving the properties of indium tin oxide thin films by the incorporation of carbon nanotubes with solution-based techniques. *Thin Solid Films* **2020**, *697*, 137844. [CrossRef]
2. Woong, S.J.; Anthony, H.F. Is indium tin oxide a suitable electrode in organic solar cells? Photovoltaic properties of interfaces in organic p/n junction photodiodes. *Appl. Phys. Lett.* **2006**, *88*, 093504.

3. Hong, C.H.; Shin, J.H.; Ju, B.K.; Kim, K.H.; Park, N.M.; Kim, B.S.; Cheong, W.S. Index-matched indium tin oxide electrodes for capacitive touch screen panel applications. *J. Nanosci. Nanotechnol.* **2013**, *13*, 7756–7759. [CrossRef]

4. Semenza, P. New transparent conductors take on ITO for touch-screen and display applications. *Inf. Disp.* **2013**, *29*, 40–42. [CrossRef]

5. Ji, H.Y.; Parida, B.; Park, S.; Kim, M.J.; Chung, S.J.; Kim, K. Enhancement effect of short-circuit currents of Si solar cells with inclusion of indium tin oxide layers on metal-semiconductor interfaces. *Jpn. J. Appl. Phys.* **2015**, *54*, 100306. [CrossRef]

6. Kenji, N.; Hiromichi, O.; Kazushige, U.; Toshio, K.; Masahiro, H.; Hideo, H. Thin-film transistor fabricated in single-crystalline transparent oxide semiconductor. *Science* **2003**, *300*, 1269–1272.

7. Hosseini, P.; Wright, C.D.; Bhaskaran, H. An optoelectronic framework enabled by low-dimensional phase-change films. *Nature* **2014**, *511*, 206–211. [CrossRef] [PubMed]

8. Carrillo, S.G.C.; Trumby, L.; Au, Y.Y.; Nagareddy, V.K.; Rodriguez-Hemandez, G.; Hosseini, P.; Rios, C.; Bhaskaran, H.; Wright, C.D. A nonvolatile phase-change metamaterial color display. *Adv. Opt. Mater.* **2019**, *7*, 41801782. [CrossRef]

9. Rios, C.; Youngblood, N.; Cheng, Z.G.; le Gallo, M.; Pernice, W.H.P.; Wright, C.D.; Sebastian, A.; Bhaskaran, H. In-memory computing on a photonic platform. *Sci. Adv.* **2019**, *5*, eaau5759. [CrossRef]

10. Madhvendra, N.T.; Kazuhito, S.; Ryoji, S.; Hiroshi, M.; Yoshiyuki, K. First-principles analysis of structural and opto-electronic properties of indium tin oxide. *J. Appl. Phys.* **2012**, *111*, 103110.

11. Tripathi, M.N.; Bahramy, M.S.; Shida, K.; Sahara, R.; Mizuseki, H.; Kawazoe, Y. Optoelectronic and magnetic properties of Mn-doped indium tin oxide: A first-principles study. *J. Appl. Phys.* **2012**, *112*, 073105. [CrossRef]

12. Bai, L.N.; Wei, Y.P.; Lian, J.S.; Jiang, Q. Stability of indium-tin-oxide and its optical properties: A first-principles study. *J. Phys. Chem. Solids* **2013**, *74*, 446–451. [CrossRef]

13. Warschkow, O.; Ellis, D.E.; Gonzalez, G.B.; Mason, T.O. Defect cluster aggregation and nonreducibility in tin-doped indium oxide. *J. Am. Chem. Soc.* **2003**, *86*, 1707–1711. [CrossRef]

14. Nadaud, N.; Lequeux, N.; Nanot, M.; Jove, J.; Roisnel, T. Structural studies of tin-doped indium oxide (ITO) and In4Sn3O12. *J. Solid State Chem.* **1998**, *135*, 140–148. [CrossRef]

15. Karazhanov, S.Z.; Ravindran, P.; Vajeeston, P.; Ulyashin, A.; Finstad, T.G.; Fjelivag, H. Phase stability electronic structure, and optical properties of indium oxide polytypes. *Phys. Rev. B* **2007**, *76*, 075129. [CrossRef]

16. McGuinness, C.; Stagarescu, C.B.; Ryan, P.J.; Downes, J.E.; Fu, D.F.; Smith, K.E.; Egdell, R.G. Influence of shallow core-level hybridization on the electronic structure of post-transition-metal oxides studied using soft X-ray emission and absorption. *Phys. Rev. B* **2003**, *68*, 165104. [CrossRef]

17. Barr, T.L.; Liu, Y.L. An X-ray photoelectron spectroscopy study of the valence band structure of indium oxides. *J. Phys. Chem. Solids* **1989**, *50*, 657–664. [CrossRef]

18. Hamberg, I.; Granqvist, C.G.; Berggren, K.F.; Sernelius, B.E.; Engstrom, L. Band-gap widening in heavily Sn-doped In2O3. *Phys. Rev. B* **1984**, *30*, 3240–3246. [CrossRef]

19. Wang, L.; Yu, L.; Wu, J.Z.; Wen, J.; Xiong, B.S. Scanning near-field optical microscopy based phase-change optical memory. *Appl. Phys. Express* **2019**, *12*, 095002. [CrossRef]

20. Rios, C.; Hosseini, P.; Wright, C.D.; Bhaskaran, H.; Pernice, W.H.P. On-chip photonic memory elements employing phase-change materials. *Adv. Mater.* **2014**, *26*, 1372–1377. [CrossRef]

21. Rios, C.; Stegmaier, M.; Hosseini, P.; Wang, D.; Scherer, T.; Wright, C.D.; Bhaskaran, H.; Pernice, W.H.P. Integrated all-photonic non-volatile multi-level memory. *Nat. Photonics* **2015**, *9*, 725–733. [CrossRef]

22. Li, X.; Youngblood, N.; Rios, C.; Cheng, Z.G.; Wright, C.D.; Pernice, W.H.P.; Bhaskaran, H. Fast and reliable storage using a 5 bit, nonvolatile photonic memory cell. *Optica* **2019**, *6*, 1–6. [CrossRef]

23. Kresse, G.; Furthmuller, J. Efficient iterative schemes for ab initio total-energy calculations using a plane-wave basis set. *Phys. Rev. B* **1996**, *54*, 11169. [CrossRef] [PubMed]

24. Kresse, G.; Hafner, J. Ab initio molecular-dynamics simulation of the liquid-metal-amorphous-semiconductor transition in germanium. *Phys. Rev. B* **1994**, *49*, 14251–14269. [CrossRef]

25. Agoston, P.; Erhart, P.; Klein, A.; Albe, K. Geometry, electronic structure and thermodynamic stability of intrinsic point defects in indium oxide. *J. Phys. Condens. Matter* **2009**, *21*, 455801. [CrossRef]

26. Kresse, G.; Hafner, J. Ab initio molecular dynamics for liquid metals. *Phys. Rev. B* **1993**, *47*, 558–561. [CrossRef]

27. Persson, K.; Berkeley, C.A. Materials Data on In2O3 (SG:206) by Materials Project (United States). 2014. Available online: https://materialsproject.org/materials/mp-22598/ (accessed on 11 November 2020). [CrossRef]

28. Kresse, G.; Furthmuller, J. Efficiency of ab initio total energy calculations for metals and semiconductors using a plane-wave basis set. *Comput. Mater. Sci.* **1996**, *6*, 15–50. [CrossRef]

29. Perdew, J.P.; Burke, K.; Ernzerhof, M. Generalized gradient approximation made simple. *Phys. Rev. Lett.* **1996**, *77*, 3865–3868. [CrossRef]

30. Kresse, G.; Joubert, D. From ultrasoft pseudopotentials to the projector augmented wave method. *Phys. Rev. B* **1999**, *59*, 1758–1775. [CrossRef]

31. Blochl, P.E. Projector augmented wave method. *Phys. Rev. B* **1994**, *50*, 17953–17979. [CrossRef]

32. Monkhorst, H.J.; Pack, J.D. Special points for Brillouin-zone integrations. *Phys. Rev. B* **1976**, *13*, 5188–5192. [CrossRef]

33. Ozaki, T.; Kino, H. Efficient projector expansion for the ab initio LCAO method. *Phys. Rev. B* **2005**, *72*, 045121. [CrossRef]

34. Ozaki, T.; Kino, H. Numerical atomic basis orbitals from H to Kr. *Phys. Rev. B* **2004**, *69*, 195113. [CrossRef]
35. Ozaki, T. Continued fraction representation of the Fermi Dirac function for large scale electronic structure calculations. *Phys. Rev. B* **2007**, *75*, 035123. [CrossRef]
36. Ozaki, T. Variationally optimized atomic orbitals for large scale electronic structures. *Phys. Rev. B* **2003**, *67*, 155108–155192. [CrossRef]
37. Segall, M.D.; Lindan, Philip, J.D.; Probert, M.J.; Pickard, C.J.; Hasnip, P.J.; Clark, S.J.; Payne, M.C. First-principles simulation: Ideas, illustrations and the CASTEP code. *J. Phys. Cond. Mat.* **2002**, *14*, 2717–2744. [CrossRef]
38. Peng, W.; Li, L.X.; Yu, S.H.; Zheng, H.R.; Yang, P. Structure, binding energy and optoelectrical properties of p-type CuI thin films: The effects of thickness. *Appl. Surf. Sci.* **2020**, *502*, 144424. [CrossRef]
39. Knickerbocker, S.A.; Kulkarni, A.K. Calculation of the figure of merit for indium tin oxide films based on basic theory. *J. Vac. Sci. Technol. A* **1995**, *13*, 1048–1052. [CrossRef]
40. Sipe, J.E.; Shkrebtii, A.I. Second-order optical response in semiconductors. *Phys. Rev. B* **2000**, *61*, 5337–5338. [CrossRef]
41. Ravindran, P.; Delin, A.; Johansson, B.; Eriksson, O.; Wills, J.M. Electronic structure, chemical bonding, and optical properties of ferroelectric and antiferroelectric NaNO$_2$. *Phys. Rev. B* **1999**, *513*, 1776–1778. [CrossRef]
42. Guo, E.-J.; Guo, H.Z.; Lu, H.B.; Jin, K.J.; He, M.; Yang, G.Z. Structure and characteristics of ultrathin indium tin oxide films. *Appl. Phys. Lett.* **2011**, *98*, 011905. [CrossRef]